DIFFUSION TENSOR IMAGING AND QUANTITATIVE TRACTOGRAPHY OF
SKELETAL MUSCLE FOR MICROSTRUCTURAL TISSUE CHARACTERIZATION

BY

ARMEN ALEX GHARIBANS

THESIS

Submitted in partial fulfillment of the requirements
for the degree of Master of Science in Mechanical Engineering
in the Graduate College of the
University of Illinois at Urbana-Champaign, 2011

Urbana, Illinois

Adviser:

Professor John G. Georgiadis

Abstract

This thesis aims to investigate the use of magnetic resonance diffusion tensor imaging (DTI) as a non-invasive tool to study the structure and organization of human skeletal muscle. By analyzing the diffusion of water molecules, DTI can uniquely probe the microstructure of skeletal muscle providing valuable information that other imaging tools cannot. The first aim is exploring the feasibility of using DTI and tractography to accurately represent muscle structure in the presence of imaging noise. Noise produces a random perturbation of the diffusion tensor, which can shift the eigenvectors and produce incorrect results. Various tractography algorithms are compared to determine which is the least susceptible to noise and the minimum signal-to-noise ratio for reliable results is established. The second aim is to use the tractography results to elucidate and quantify a 3D fabric structure to ultimately determine muscle quality objectively. Tracking of the secondary eigenvector, novel to the DTI field, is introduced and investigated.

Acknowledgements

I am extremely grateful to my adviser, John Georgiadis, for all of his guidance and support. When I first moved to Illinois for graduate school, I was confused and hardly knew anything about doing scientific research. He went above and beyond his duties as an adviser and taught me how to be a true researcher. I also want to thank my group members, especially Curtis Johnson, who has been there to answer all of my questions and concerns regardless of the time of day or his personal workload. I would not have been able to finish this work without the continuous support and love of my girlfriend, Sarah, my sister, Linda, and especially my parents, Edmond and Armineh.

Table of Contents

List of Tables

List of Figures

Chapter 1

Introduction

Diffusion tensor imaging (DTI) of skeletal muscle coupled with tractography has been used successfully to visualize three-dimensional muscle structure *in vivo* [1, 2]. Restricted diffusion in the tissue allows for muscle fibers to be tracked using the first eigenvector of the diffusion tensor. Various deterministic methods of tractography were originally proposed and implemented for tracking axons in the brain [3-6], and the systematic application of the same methods in skeletal muscle has only recently been documented [1, 2, 7-10].

The complexity of the organization of skeletal muscle has made it an interesting and active research area. The organization of the muscle fibers, the ability of fibers to produce contractile force, and the transmission of force from the muscle fibers to the skeleton via connective tissue all contribute to overall muscle quality. The decline in muscle strength and muscle mass with age (sarcopenia) is well documented [11, 12] and is associated with a deterioration of health status and functional abilities [13, 14]. DTI is capable of non-invasively probing the microstructure of skeletal muscle, providing valuable information that could be used to quantify muscle quality.

1.1 Skeletal Muscle

Skeletal muscle is a complex biological material that has a hierarchical organization of muscle fibers, and an extracellular matrix (ECM) consisting of the epimysium, perimysium, and endomysium. A transverse section of a typical muscle has a diameter from one to ten

centimeters and consists of bundles of fascicles (1-2 mm in diameter), which are composed of bundles of myofibers (10-100 μm in diameter). Sophisticated biomechanical models have been implemented to find the connection between the 3D fiber architecture and function [15-18], and it has been hypothesized that the division of the muscle into fascicles is to accommodate for non-uniform strains during contraction and elongation [19]. Studies have shown that each fascicle shortens uniformly, but the muscle as a whole exhibits non-uniform strains during contraction and the fascicles are able to slide past one another [20]. Fascicles are therefore able to achieve their optimal lengths at different overall muscle lengths. It has also been observed that distal fascicles tend to shorten more and act at greater pennation angles than the more proximal fascicles in the human gastrocnemius during walking [21].

Skeletal muscle can be described as a collagen fiber-reinforced composite. The connective tissue is organized as follows: the whole muscle is surrounded by the epimysium, the fascicles are delineated by the perimysium and the myocytes are separated by the endomysium. The ECM has at least three functions: (1) to provide a framework for binding muscle fibers together to ensure their proper alignment, (2) to transmit forces, either from active muscle contraction or passively imposed ones, and (3) to provide lubricated surfaces between muscle fibers and fascicles, thus enabling the muscle to change shape [22]. The mechanical properties of skeletal muscle depend on both the properties of muscle fibers and the ECM, and the interaction between the two. Due to the nature of skeletal muscle, direct measurements are not possible, but many indirect studies and analyses have shown that the ECM is an important part of force transmission during muscle contraction [23-26].

1.1.1 Mechanical Role of the Endomysium

The muscle fibers within a fascicle are surrounded and connected by the endomysium. The

structure of the endomysium has been shown to be generally equivalent for all skeletal muscles within and across species [27]. Many of the muscle fibers end within the muscle and do not connect to the tendon directly, thus necessitating a force transmission pathway via the endomysium [26]. The planar network of the collagen fibers appears to be randomly distributed when viewed on a large scale, but detailed analysis has shown that the network is not truly random and that there is a preferred direction that changes with muscle elongation [23]. The organization of collagen fibers in the endomysium suggests reorientation due to transmission of forces.

Any linkage transmitting force from the muscle fibers to the tendon must be non-compliant (i.e. of high stiffness) in order to be efficient. Experimental force-length measurements have shown that the passive tensile properties of relaxed muscle were derived mainly from the elastic resistance of the myofibrils and not the connective tissue (i.e. the myofibrils were much stiffer in tension than the connective tissue) [28]. In another study, it was determined that the non-linear tensile properties of the endomysium under normal physiological conditions were too compliant in tension to act as efficient force transmitters in tension [23]. In light of these findings, the concept of shear force transmission between adjacent muscle fibers in the endomysium was introduced [29]. Figure 1.1 is a simple model consisting of two parallel muscle cells with the endomysium sandwiched between them. Assuming the simplest linear models, the shear stress (F/LW) and the shear strain (ΔL/H) in the endomysium can be related to the shear modulus (G) (Eq. 1.1):

$$G = \frac{F}{\Delta L} \frac{H}{LW}$$

(1.1)

where

- F is the force generated along the direction of the muscle action

- *W* is the width of the muscle fiber
- *L* is the length of the muscle fiber
- Δ*L* is the change in length of the assembly
- *H* is the thickness of the endomysium
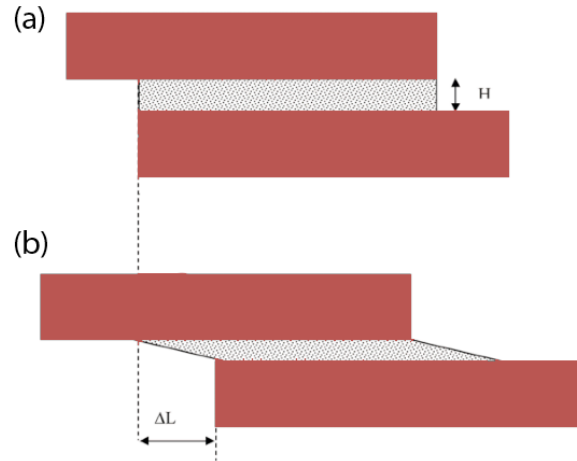
Figure 1.1: The shear force transmission between muscle fibers (red) via the endomysium.

If the change in length (ΔL) is approximated as the longitudinal tensile displacement, the apparent tensile modulus (E_{app}) becomes (Eq. 1.2):

$$E_{app} = G\left(\frac{L}{H}\right)^2$$

(1.2)

The length of the muscle fiber (L) is orders of magnitude larger than the thickness (H), making the term $(L/H)^2$ very large. Therefore, the apparent longitudinal modulus is much greater than the true shear modulus. Because the endomysium is so thin, even large shear strains would only result in minute tensile elongations. If the apparent longitudinal modulus is represented in series with the fibers, the modulus of the composite structure (E_c) is (Eq. 1.3):

$$\frac{1}{E_c} = \frac{1}{E_f} + \frac{1}{E_{app}}$$

(1.3)

and is dictated by the fiber modulus E_f, because E_{app} is many orders of magnitude higher. This shear force transmission pathway from one muscle cell to its neighbors is highly efficient. Also,

because it has low tensile stiffness, it does not restrict changes in muscle fiber length and diameter during muscle contraction [30].

1.1.2   Mechanical Role of the Perimysium

Unlike the endomysium, the perimysium has large variations in quantity and organization from one muscle group to another even in the same person [31]. There is far more perimysium than endomysium in the muscle. It has been determined that the ratio of the dry mass of perimysium to that of endomysium ranges between 2.8:1 and 64:1 in different muscles [32]. The relatively small variation in the endomysium compared with perimysium content between muscles could indicate some of the functional differences between the muscle groups. The anatomical arrangement of the connective tissue at each level of organization influences the function of the muscle.

Interestingly, the collagen fibers in the perimysium usually orient between 45 to 60 degrees to the long axis of the muscle fibers in their relaxed state [22]. Well defined contact regions between the endomysium and perimysium have also been observed and named the perimysial junctional plates (PJPs), as seen in Figure 1.2 [33]. These sites have been hypothesized to be focal regions for delivery of tension during muscle contraction. To test the possibility of tensile force transmission via the perimysium, it has been experimentally shown that cutting of the aponeurosis in a pennate muscle did not prevent tension generation further along towards the tendon [25]. Also, in a separate study it was clearly demonstrated that the perimysium could transmit force if tendons from distinct parts of the extensor digitorum longus muscle were cut [24].
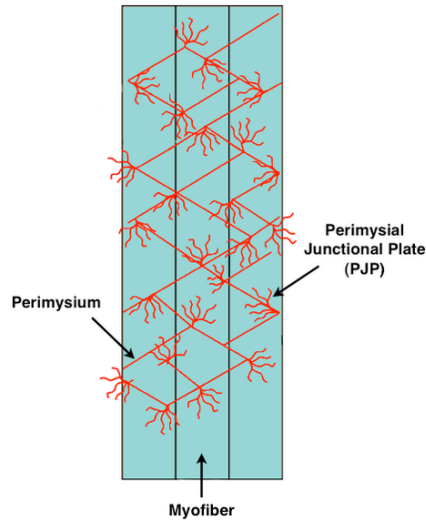
Figure 1.2: Schematic of the perimysium organization in skeletal muscle showing the attachment at the myofiber surface via perimysium junctional plates (PJPs) [33].

Although a lot of evidence seems to point to lateral force transmission via the perimysium in tension, the experiments were conducted at very high loads, possibly giving inaccurate results. Under sufficient stress, the collagen fibers of the perimysium begin to orient parallel to the stress direction. The stretching and reorientation of the perimysium makes it much stiffer and able to transmit tensile force. Scanning electron microscope images have shown that the perimysium has an organized crimped structure [22]. The crimped structure of the perimysium makes it very compliant in tension under normal physiological conditions allowing the muscle to change shape, thus rendering it unfeasible for tensile force transmission [30]. It can also be suggested that the perimysium could transmit force generated in fascicles to neighboring fascicles by shear, similar to the endomysium described above. Because the perimysium is significantly thicker than the endomysium, even if the shear modulus of the perimysium was within an order of magnitude of the endomysium, the perimysium would still be much more compliant, making it an inefficient force transmission pathway [34].

6

Although strong efforts have been made to demonstrate the mechanical role of the perimysium as a force transmission pathway during active contraction of the muscle, an accepted model has yet to be derived. There are alternate theories on the role of the perimysium being strictly for distributing passive forces imposed on the muscle and preventing over-stretching of the muscle fascicles [35].

1.2 Diffusion Tensor Imaging

Diffusion weighted imaging is (DWI) is a magnetic resonance imaging (MRI) technique that quantifies the diffusion of water molecules *in vivo*. It can provide information to help characterize tissue composition, tissue microstructure and architectural organization, and physical properties of tissue [36, 37]. In unrestricted Brownian motion, such as in a cup of water, the water molecules diffuse freely in all directions. By introducing diffusion barriers, the water motion is becomes restricted in certain directions as it can no longer move through the barrier [38, 39]. The basic concept of DWI is that barriers in biological tissue, including cell membranes, myelin and connective tissue, restrict the diffusion of water, thus generating a direction-specific contrast mechanism in MRI that reflects the underlying tissue microstructure.

Diffusion weighted MRI can be used to calculate the diffusion coefficient of water molecules in a specified direction. When a magnetic field gradient is applied, depending on the location within the gradient, the water molecules experience different field strengths and resonate at different frequencies. If no diffusion occurs and an opposite gradient is applied, all of the molecules return to being perfectly in phase, and the entire signal is recovered. The dephasing gradient essentially "tags" the locations of the water molecules. If the molecules diffuse in the time between the dephasing and rephasing gradients, the molecules that have moved can be detected because they have different phases from the other, stationary molecules,

and the signal is not completely recovered. The resulting MRI signal, S, is related to the

diffusion coefficient by the formula (Eq. 1.4):

$$S = S_0 e^{-bD}; \quad b = \gamma^2 G^2 \delta^2 \left(\Delta - \delta / 3 \right)$$

(1.4)

where

- S_0 is the signal intensity in the absence of diffusion-weighting
- D is the diffusion coefficient
- γ is the gyromagnetic ratio (2.765 x 10^8 rad/s)
- δ is the gradient length
- Δ is the time between gradients
- G is the gradient strength

An increase in diffusivity or diffusion-weighting (increase in b) causes increased dephasing of

the protons, resulting in a decreased MRI signal. In diffusion tensor imaging (DTI), magnetic

gradients are applied in at least six non-collinear directions, allowing for a symmetric diffusion

tensor can be computed for each voxel. An image with no diffusion weighting, referred to as the

b_0 image, is also necessary for calculating the diffusion tensor at each voxel as it is used as the

baseline signal S_0. The tensor can be represented as three eigenvalues (λ_1, λ_2, λ_3) with their

corresponding eigenvectors (e_1, e_2, e_3) by simple matrix decomposition.

1.2.1 Tractography

The eigenvectors of the diffusion tensor create a vector field, which contains information about

muscle structure that tractography algorithms attempt to extract. Thus far, tractography has

mainly been used as a visualization tool for skeletal muscle. The only quantitative application of

tractography has been the measurement of the pennation angle of muscle fibers [1, 7].

Generally, tractography algorithms can be divided into two main categories: deterministic

and probabilistic [40]. The deterministic approach is based on tract propagation and provides

only one solution from a given seed point. On the other hand, the probabilistic technique is

based on energy minimization, where two arbitrary points are selected and the most probable path to connect the two points is determined [41-44]. Deterministic tractography is the simpler of the two and also requires significantly less computing power.

Probabilistic tractography was created was to address specific challenges in the brain. An imaging voxel for DTI in the brain is on the order of 1-2 mm, while the white mater fibers have a diameter on the order of 1 μm. Therefore, there can be many bundles of axons in a single voxel that do not go in the same direction. To further complicate things, the bundles can even cross, split or merge within a voxel. Fortunately, these challenges do not exist in skeletal muscle, where the muscle fibers are coherently organized and do not cross, making deterministic algorithms more favorable.

In this work, two software packages were employed to process and visualize DTI data. Diffusion Toolkit (version 0.6.1) is a software package that performs data reconstruction and tractography on DTI data [45]. TrackVis (version 0.5.1) is also included in the package, which is used to visualize and analyze the tractography results of Diffusion Toolkit. Diffusion Toolkit is capable of performing tractography using four deterministic algorithms: Fiber Assignment by Continuous Tracking (FACT) [3], interpolated streamline [4], second-order Runge-Kutta [5] and tensorline [6].

For all four of the algorithms, tracking is initiated from seed points, which can be at the center of each voxel or randomly placed in each voxel. The use of multiple seed points per voxel can also be specified. For the FACT algorithm, illustrated in Figure 1.3, after initiation the tracking proceeds according to the vector direction in each voxel. When the track enters the neighboring voxel, its direction changes to that of the neighbor. In each voxel, the direction of all the tracks within that voxel is parallel to the vector direction. The FACT algorithm uses

variable step sizes, which depend on the length of the trajectory needed to pass through a voxel.

The interpolated streamline algorithm is very similar to the FACT algorithm, but a small, predefined step size is used, typically 0.5mm, and at each step the eigenvector is interpolated from neighboring voxels. The smooth curvature resulting from using a smaller step size is demonstrated in Figure 1.4.
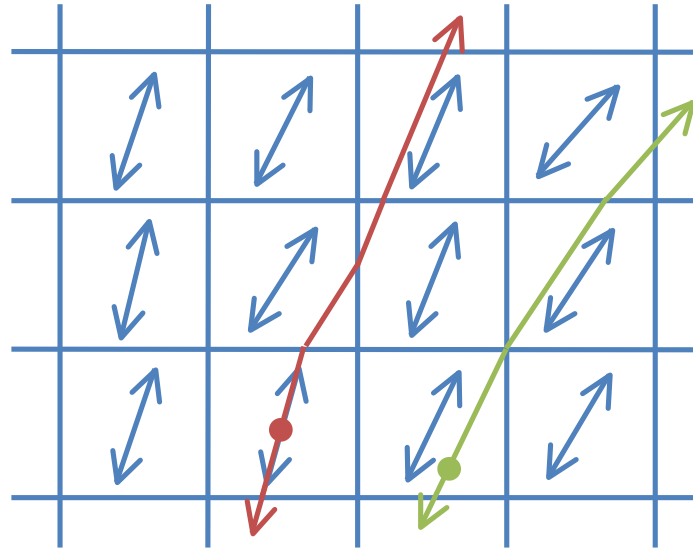

Figure 1.3: Illustration of FACT algorithm showing track propagation from a seed point in the center of a voxel (red circle) and a random seed in a voxel (green circle).
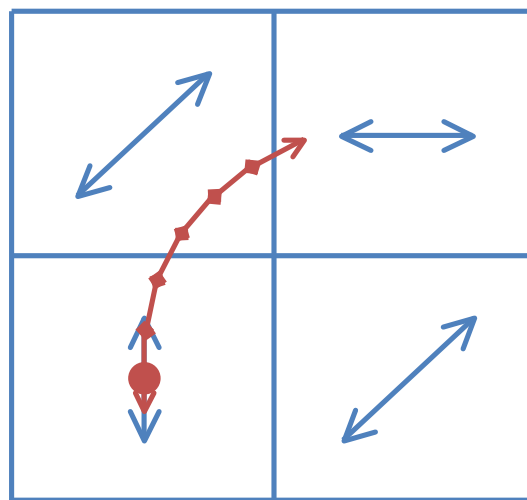

Figure 1.4: Illustration of interpolated streamline algorithm (constant step size) showing track propagation from a seed point in the center of a voxel (red circle).

The track can also be represented as a vector, r(s), parameterized by the arc length, s, of the trajectory. The tangent vector, t(s) is equated to the unit eigenvector, e_1, calculated at position r(s): t(s) = e_1 r(s). Therefore, the differential equation with initial condition (Eq. 1.5):

$$\frac{d\mathrm{r}(s)}{ds} = e_1\big(\mathrm{r}(s)\big); \quad \mathrm{r}(0) = \mathrm{r}_0$$

(1.5)

can be solved using the second-order Runge-Kutta technique, which is preferred to Euler's method because its estimates of higher derivatives of r(s) are more reliable.

The tensorline algorithm uses a very different approach. Instead of simply tracking the primary eigenvector and ignoring the secondary and tertiary eigenvectors, the entire diffusion tensor is used to deflect the incoming vector (v_{in}) direction, which can be described as (Eq. 1.6):

$$v_{in} = \alpha_1 e_1 + \alpha_2 e_2 + \alpha_3 e_3$$

(1.6)

where α_1, α_2 and α_3 are relative vector weightings. The outgoing vector (v_{out}) direction can then be computed using the equation (Eq. 1.7):

$$v_{out} = \lambda_1 \left(\alpha_1 e_1 + \frac{\lambda_2}{\lambda_1} \alpha_2 e_2 + \frac{\lambda_3}{\lambda_1} \alpha_3 e_3 \right).$$

(1.7)

For a highly anisotropic diffusion tensor ($\lambda_1 \gg \lambda_2, \lambda_3$), the output vector is deflected towards the direction of the primary eigenvector. For an oblate shaped diffusion tensor ($\lambda_1 \approx \lambda_2 \gg \lambda_3$), both the primary and secondary eigenvectors contribute to the deflection. For an isotropic tensor ($\lambda_1 \approx \lambda_2 \approx \lambda_3$), the outgoing vector is the same as the incoming vector.

All of the tractography algorithms used by Diffusion Toolkit utilize the same termination criteria for a track. The tracks terminate if a predefined angle is exceeded from one step to the next. This curvature criterion inhibits the trajectories from following unlikely pathways.

1.3   Objectives

The following chapters attempt to verify the notion that DTI can be used to establish a quantitative measure for muscle quality.

In chapter two, we investigate the effects of noise on tractography in skeletal muscle. To be able to use tractography as a quantitative tool, the reproducibility of the results need to be assessed. The aim of this chapter is simply to provide confidence in the tractography output.

DTI has been used to study muscle structure by tracking the primary eigenvector of the diffusion tensor. In chapter three, we take this a step further by tracking both the primary and secondary eigenvectors to elucidate a fabric structure. Various hints from literature point to the fabric structure being linked to the organization of fascicles in the muscle. The aim of this chapter is to establish the existence of the fabric DTI reconstruction in skeletal muscle and quantify the organization of the fabric to ultimately relate it to muscle quality.

Chapter 2

The Effect of Diffusion Tensor Imaging SNR on Skeletal Muscle Tractography

2.1   Introduction

A major challenge in skeletal muscle tractography is the low signal-to-noise ratio (SNR) associated with the images. Diffusion tensor imaging of skeletal muscle is an inherently noisy imaging method owing to long echo times, necessity of echo-planar imaging, and short T2-relaxation times in the tissue. The noise from DTI corrupts the solution of the eigenvalue problem, and can shift the direction of the eigenvectors enough for the tracks to deviate from real fiber orientations. Due to the nature of deterministic track propagation, the noise errors accumulate as the propagation becomes longer. Though post-processing noise removal [46-48] and regularization filter algorithms [49, 50] have been developed to combat this issue, their efficacy remains ambiguous. When attempting to utilize deterministic tractography in the muscle in a quantitative way, it is important to understand how SNR affects tractography to be able to estimate the reliability of the results [10]. In this chapter the effects of SNR on deterministic tractography of skeletal muscle were investigated.

2.2   Theory

The calculation of the signal-to-noise ratio (SNR) for diffusion-weighted images (DWIs) is not straightforward, because the DWIs and b_0 images (no diffusion weighting) have different signal intensity and noise profiles. The DWIs have lower signal intensity and the signal also varies for

different anatomical locations based on the direction of diffusion and applied diffusion gradients. Therefore, the SNR of the b_0 image is typically reported and is often calculated using the "difference method" [51]. First, using two sequential b_0 images, the average and difference images are computed and a region-of-interest (ROI) is selected. Then, SNR is calculated as the mean value of the average image divided by the standard deviation over the values of the difference image in the ROI (Eq. 2.1).

$$\text{SNR}(\text{ROI}) = \frac{\text{mean}(\text{average image})}{\text{std}(\text{difference image})}$$

(2.1)

The SNR can be assumed to scale with the square root of the number of averages (i.e. doubling the number of averages increases the SNR by $\sqrt{2}$).

An important limitation of this method is the size of the ROI and its placement. Figure 2.1 shows that by slightly shifting the ROI location, the SNR calculation can be completely different. Therefore, this method cannot be used when trying to determine the minimum SNR necessary for a certain quantitative calculations. Also, if the SNR of many subjects in a study is to be computed, hand selecting the ROI can be extremely inefficient and time consuming.
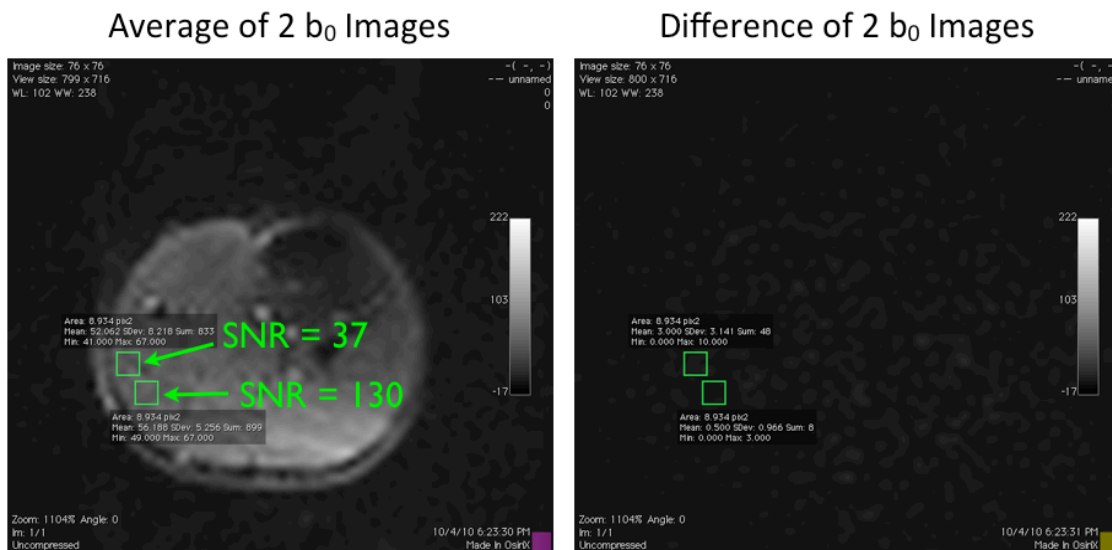

Figure 2.1: Dependence of SNR calculation on user defined ROI location (green box).

2.3   Methods

2.3.1   Calculating Signal-to-Noise Ratio (SNR)

It was necessary to create an automated SNR calculation algorithm that did not include the user selection of the ROI. An ROI was already being drawn for tractography, which included all the slices of a single muscle; the same ROI was used for calculating the SNR. Calculating the mean of the signal and the standard deviation of the noise over the entire muscle eliminated the variability of hand selecting a small ROI and produced more consistent results. As long as the same method was used to compute SNR, different scans could be compared. To test the accuracy of this method, the SNR of the DTI scans at different b-values ($300 - 1000$ s/mm^2) were compared for the b_0 and diffusion-weighted images. All the scans were acquired consecutively in one scan session.

An algorithm was also written to quickly visualize the SNR distribution in the muscle. By breaking up the image into nine voxel tiles, an SNR map was computed and plotted.

2.3.2   DTI and Tractography

The effects of DTI SNR on tractography in skeletal muscle were investigated by comparing a few geometrical parameters of the reconstructed tracks from various tracking algorithms.

The study was performed on four healthy subjects (age: 23 ± 2 years). The volunteers were in supine position with legs in the relaxed state, placed parallel to the magnetic field, feet first. DTI data was acquired on the left calf of two of the subjects, and the left thigh of the other two. All data was collected on a 3T full-body Siemens Trio scanner (Siemens Medical Systems, Erlangen, Germany). Diffusion-weighted images were acquired using a single-shot twice-refocused spin-echo EPI sequence with the following parameters: TR/TE = 3000/71 ms, FOV =

25x25 cm^2, slice thickness = 10 mm, matrix = 76x76, and seven axial slices. Water excitation

was performed using a spatial-spectral RF pulse to remove the signal contribution from fat.

Diffusion weighted gradients were applied along 30 non-collinear directions with a nominal b-

value of 550 s/mm^2. Two of the DTI scans had 30 averages (scan time ~ 45 min) and the other

two had 10 averages (scan time ~ 15 min). These acquisitions were chose so as to get a range of

SNR values for comparison. By varying the number of DTI averages used for tractography,

different SNR levels were achieved. The overall range of the SNR analyzed was 5.1 to 51.7.

Scanning was performed using a combination of an eight-channel spine coil and a flexible body

matrix surface coil. Differences in the DTI acquisition for each subject are outlined in Table 2.1

Table 2.1: DTI acquisition and SNR range for each subject.

Subject	Muscle	Number of Averages	SNR Range
1	Vastus Lateralis	10	5.1 – 16.1
2	Vastus Lateralis	30	6.5 – 35.4
3	Gastrocnemius Medialis	30	9.4 – 51.7
4	Gastrocnemius Medialis	10	7.6 – 24.1

Tractography of the primary and secondary eigenvectors were performed with four

deterministic tractography methods: FACT [3], interpolated streamline [4], second-order Runge-

Kutta [5], and tensorline [6]. During tractography, if a predefined angle is exceeded from one

step to the next the track propagation is terminated. The angle criterions for primary and

secondary tracks were determined qualitatively in order to properly reflect muscle anatomy and

are listed in Table 2.2. FACT uses a larger variable step size while the other three algorithms use

a constant step size of 0.5mm, which results in the different angle criterions.

Table 2.2: Track termination angle criterions used for different tractography algorithms.

Tractography Method	Primary Tracks	Secondary Tracks
FACT	45º	50º
Interpolated Streamline	25º	30º
Second-Order Runge-Kutta	25º	30º
Tensorline	25º	30º

Both primary and secondary tracks were seeded at the center of each voxel to avoid the variability from using random seed points. A B-spline filter was applied to smooth the tracts, and a minimum tract length of 15mm was used in an attempt to eliminate spurious tracts. A ROI was hand-drawn containing the entire muscle being studied and all data outside the muscle was removed.

The metrics used for comparison were number of tracks drawn, mean track length (mm), and the angle of each track segment relative to the z-direction. These metrics were chosen to reflect major differences in the tractography results.

2.4   Results and Discussion

Figure 2.2 is a plot of the SNR computed from the b_0 and diffusion-weighted images at different b-values. The average SNR for the b_0 images was 14.3 ± 0.7. The small variation in computed SNR for different b-values showed that the SNR calculation was robust. Since there are no gradients applied when acquiring the b_0 image, the different b-values do not have any effect on the SNR. On the other hand, a negative exponential relationship exists between the signal intensity and b-value for DWIs (Eq. 1.4) and the Gaussian noise does not dependent on b-value, as seen in Figure 2.3. The calculated SNR for the diffusion-weighted images also demonstrated

a similar relationship with increasing b-value with the same slope, which further validated the SNR calculation method.
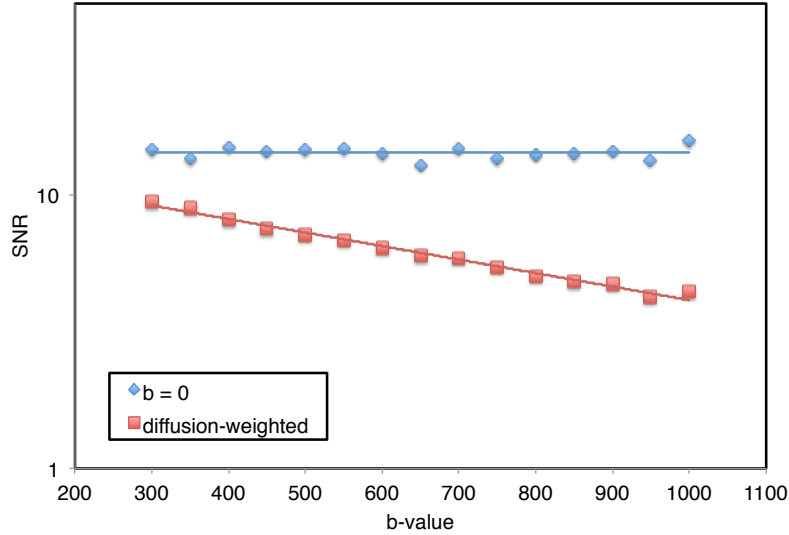
Figure 2.2: SNR computed at different b-values for b_0 and diffusion-weighted images.
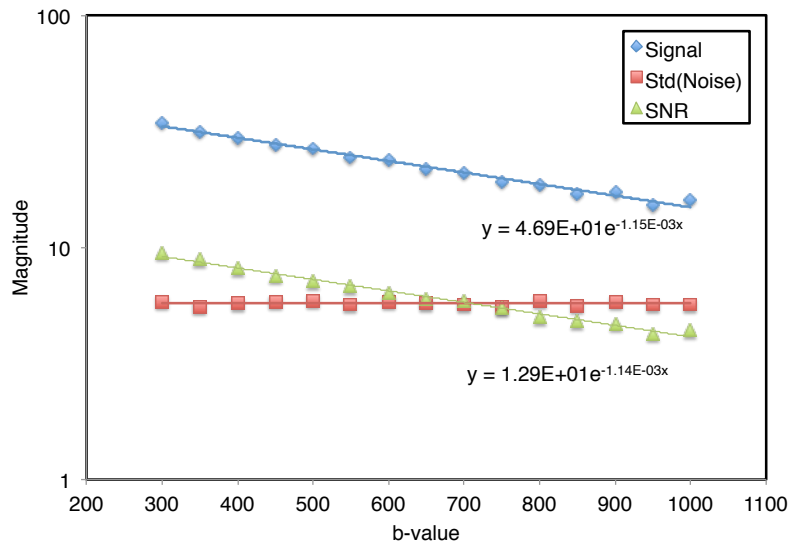

Figure 2.3: Plot of the total signal, noise and SNR for diffusion-weighted images at different b-values.

Figure 2.4 is an example of an SNR map for the thigh, showing a relatively uniform SNR distribution. The SNR map is useful in checking SNR consistency throughout the image. If certain regions have significantly lower SNR than others, the discrepancy could be investigated.

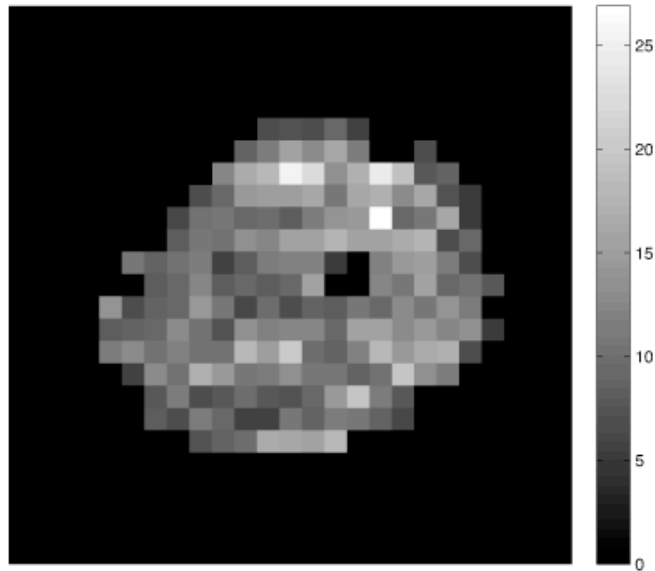The SNR map is an efficient way to check the overall quality of a DTI scan.

Figure 2.4: SNR map of thigh used for quality assurance.

Figures 2.5 through 2.8 shows the plots of the metrics versus SNR for the primary and secondary tracks of the four subjects. The plots indicate the measures from a single method start to converge at various SNR values. The only difference in the acquisition between subjects two and three was the muscle being imaged. It should be noted that the SNR of the thigh muscles were significantly lower than that of the calf. This can potentially be related to the larger size of the thigh, resulting in the muscle being at a farther distance from the spine coil.

Plot C in Figures 2.5 through 2.8 is a rough estimate of the pennation angle, which is significantly higher for the vastus lateralis than the gastrocnemius medialis. The anisotropy of the voxel size (3mm x 3mm x 10mm) can make it more difficult to track the muscle fibers at higher pennation angles, resulting in the first two subjects converging at higher SNR. It is observed that the four algorithms do not converge to the same angle, with plot C in Figure 2.6 (Subject 2) having the most discrepancy. This appears to be a limitation of deterministic tractography that has not yet been explored.

19

Figure 2.9 shows the primary tracks of Subject 1 at low SNR. The difference between FACT and interpolated streamline can clearly be seen. The tractography results of the second-order Runge-Kutta and Tensorline algorithms are qualitatively similar and demonstrate equivalent convergence patterns in Figures 2.5 through 2.8. The two algorithms actually utilize very different methods of deriving the tracks and their resemblance is most likely coincidental.

For all four subjects and tractography algorithms, the secondary tracks require higher SNR for convergence. This is most noticeable when comparing plots A and D of Figure 2.5 (Subject 1), where the primary tracks are already starting to converge at 16 SNR and the secondary tracks are still increasing. A minimum of around 35 SNR is required for convergence of the secondary tracks for all four algorithms. There are multiple explanations as to the discrepancy between the primary and secondary tracks. The secondary tracks are affected more by noise because the secondary eigenvalue is smaller in magnitude and requires less noise to converge. Also, there is significantly higher in plane (3mm x 3 mm) versus out of plane (3mm x 10mm) resolution, which favors the primary tracks.

All four tractography algorithms showed the same trends. For the primary tracks, interpolated streamline converged at around 15 SNR and showed the least variation, while the other three algorithms converged at around 20 SNR. FACT, compared to the other three methods, seemed to be affected by noise the most because the step size is based on the voxel size, which is fairly large in the case of skeletal muscle. On the other hand, the interpolated streamline method calculates the diffusion tensor after each 0.5 mm step by interpolated from the neighboring voxels, similar to applying a regularization filter to the data before tractography, and was, not surprisingly, the least susceptible to noise.

20

Figure 2.5: Subject 1 repeatability metrics plotted against SNR for primary and secondary tracks. (Muscle: vastus lateralis, Number of Averages: 10, SNR Range: 5.1 – 16.1)

Figure 2.6: Subject 2 repeatability metrics plotted against SNR for primary and secondary tracks. (Muscle: vastus lateralis, Number of Averages: 30, SNR Range: 6.5 − 35.4)
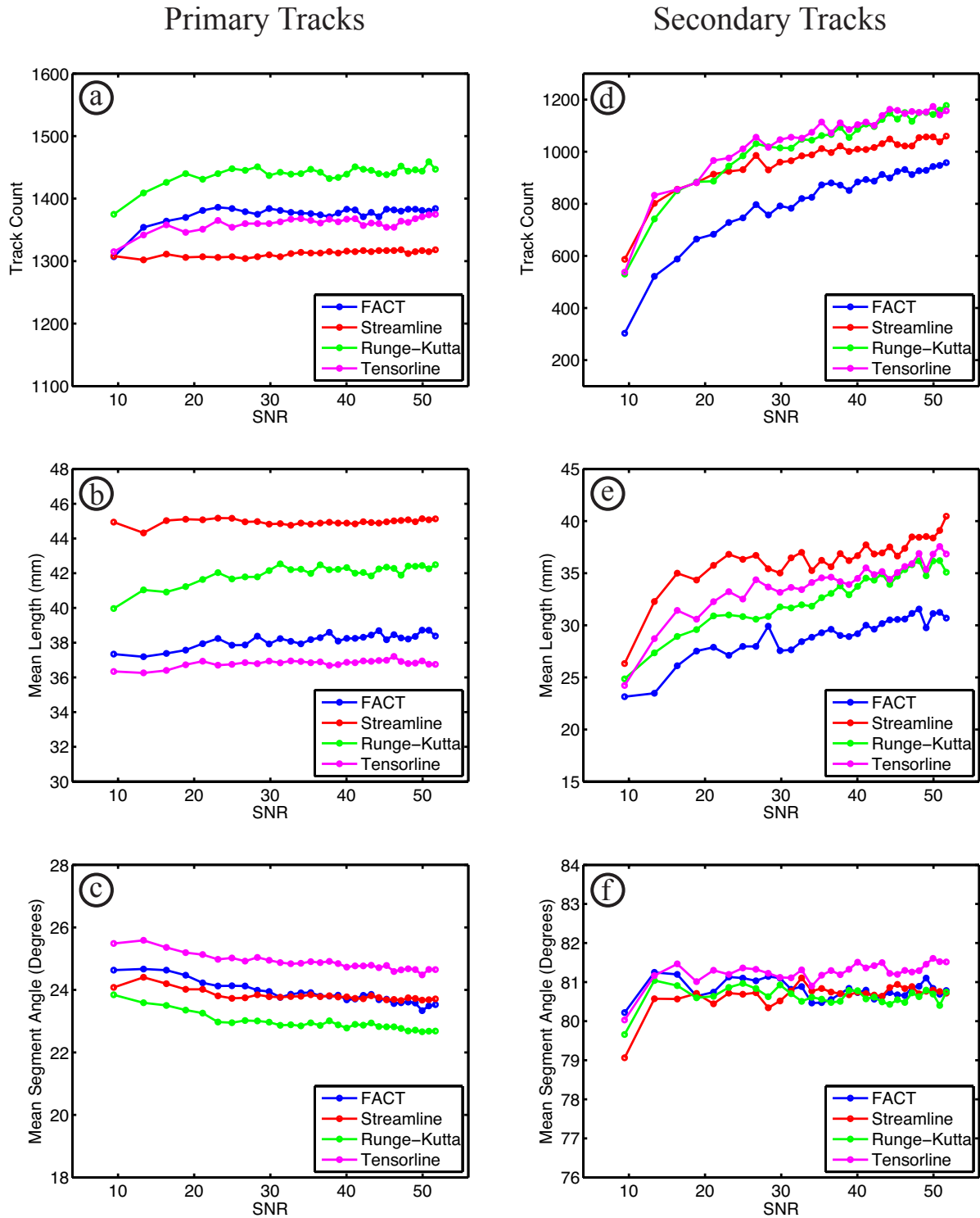
Figure 2.7: Subject 3 repeatability metrics plotted against SNR for primary and secondary tracks. (Muscle: gastrocnemius medialis, Number of Averages: 30, SNR Range: 9.4 – 51.7)
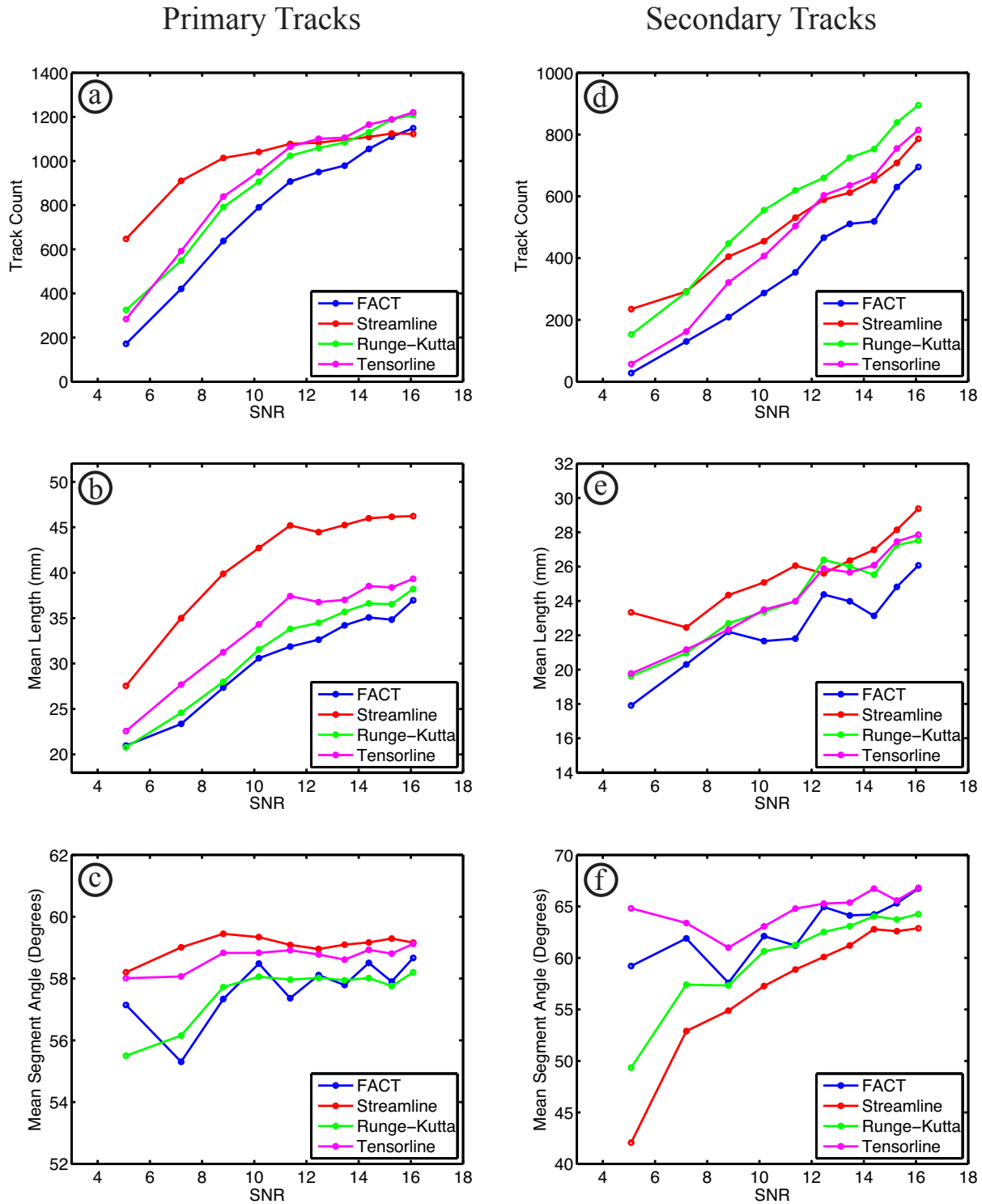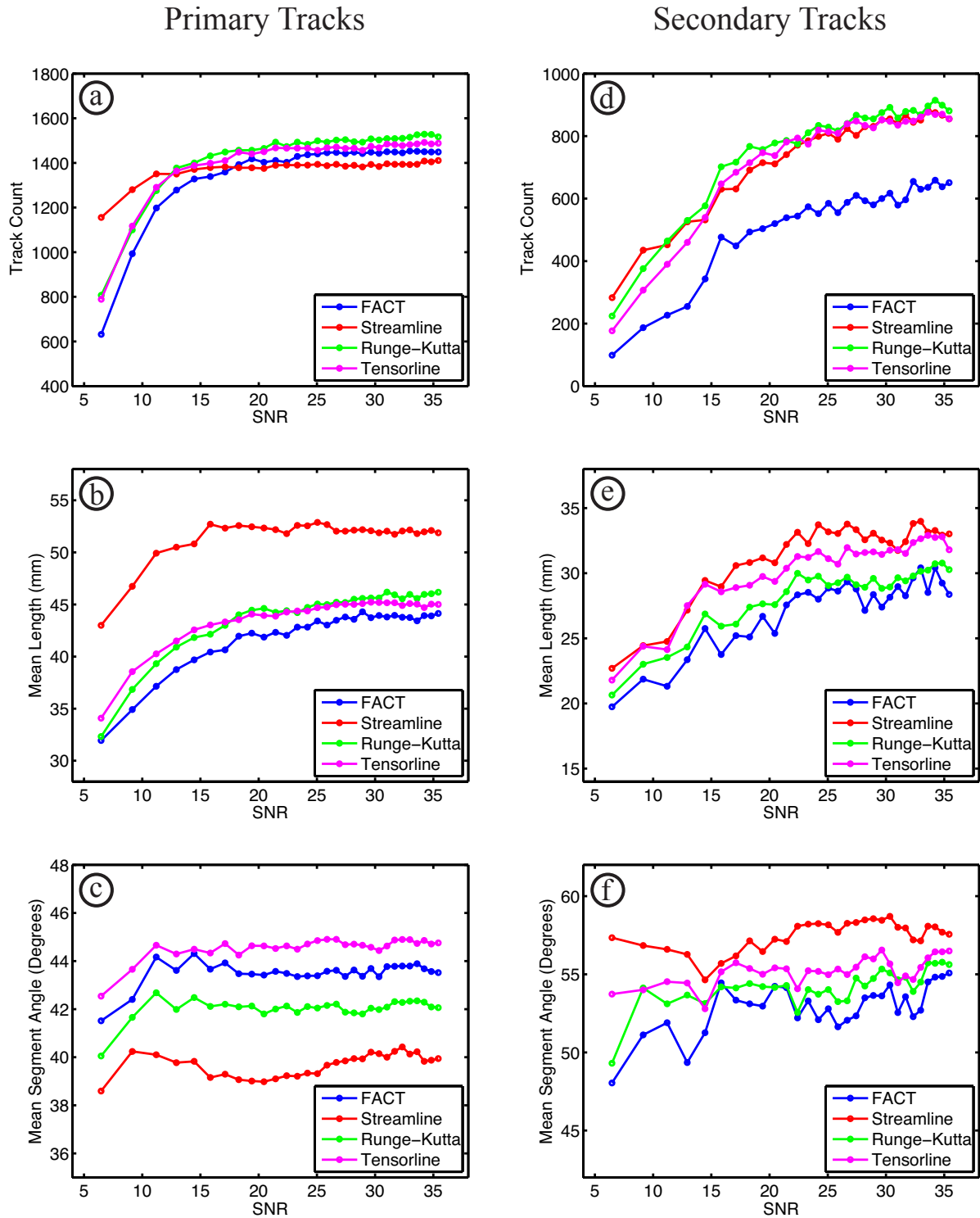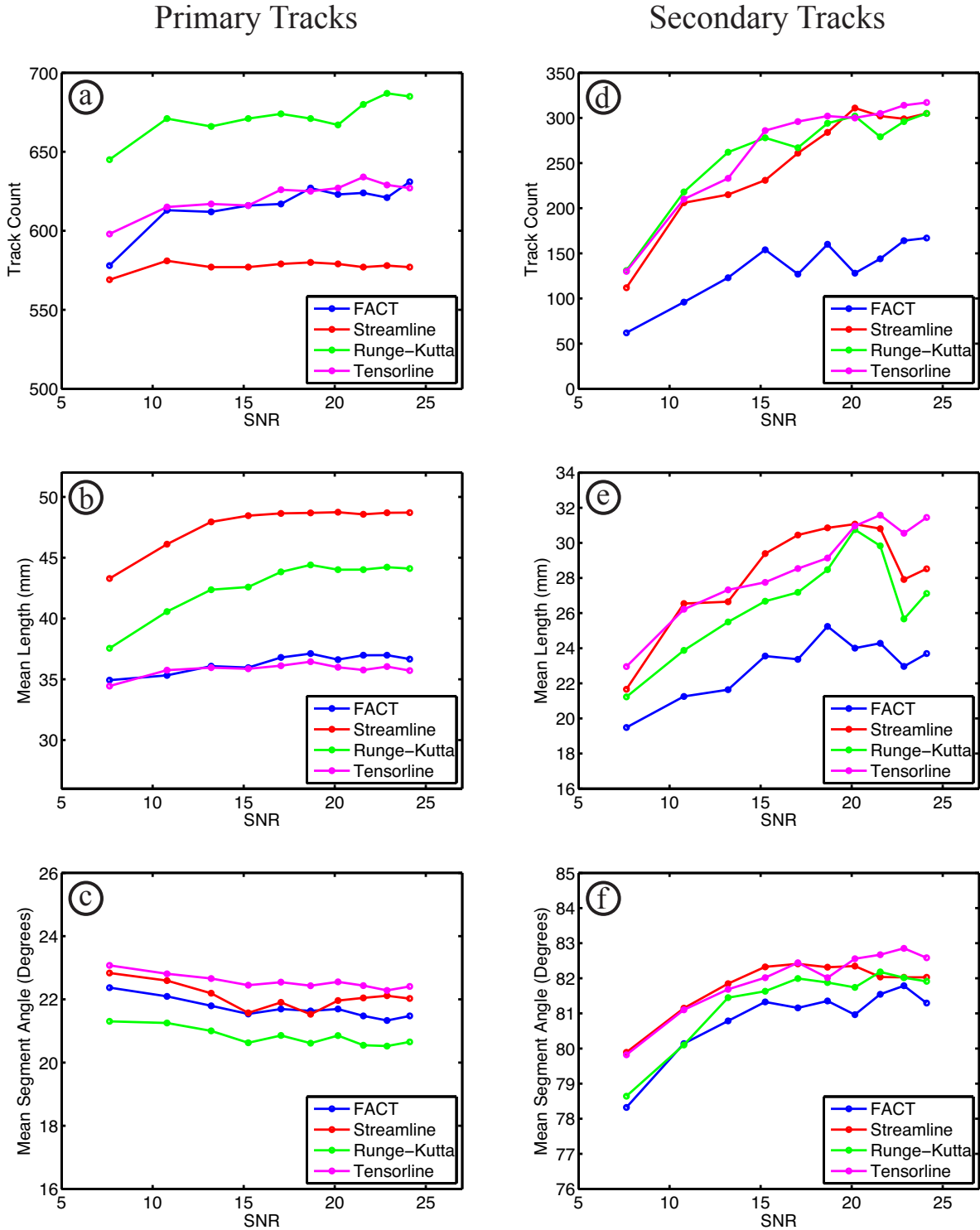
Figure 2.8: Subject 4 repeatability metrics plotted against SNR for primary and secondary tracks. (Muscle: gastrocnemius medialis, Number of Averages: 10, SNR Range: 7.6 – 24.1)
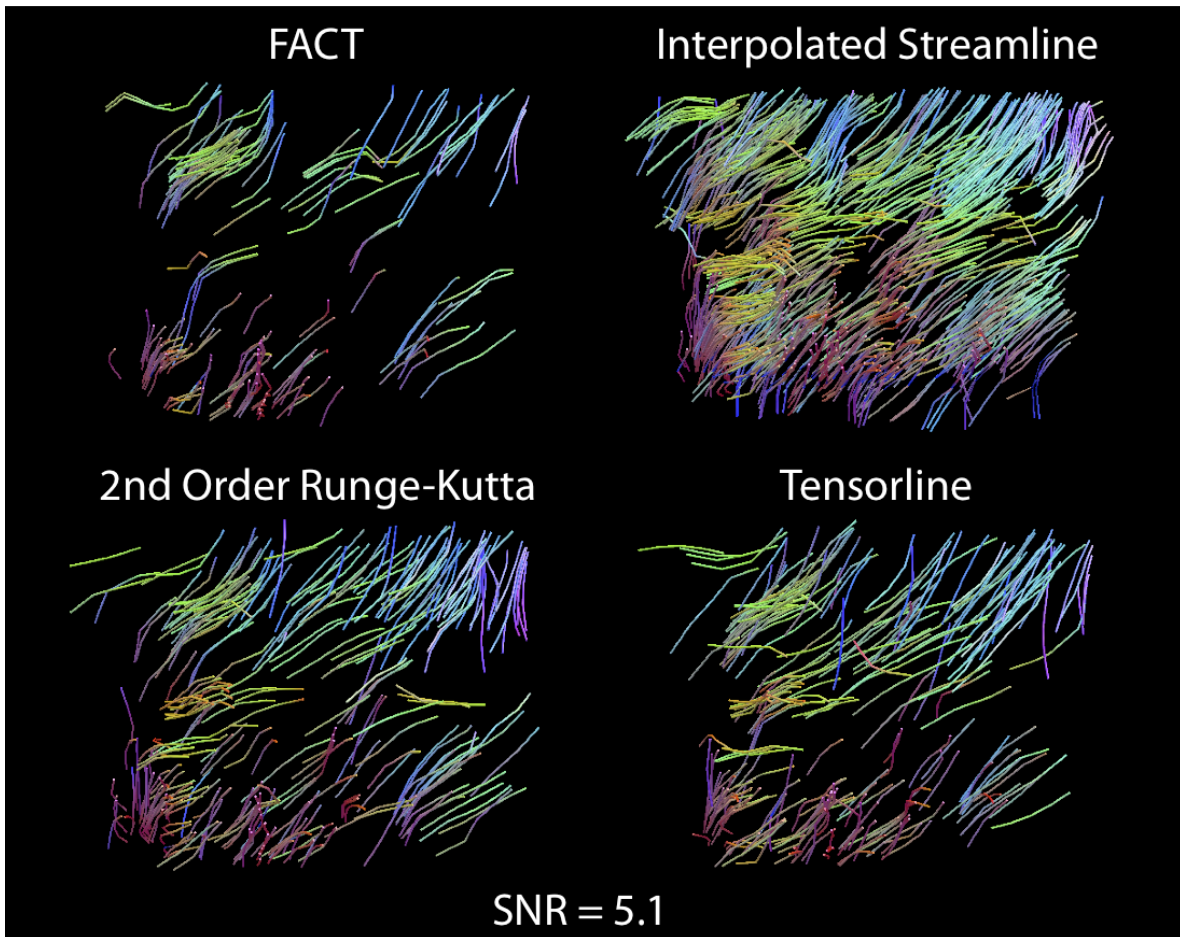
Figure 2.9: Qualitative differences in the four tractography algorithms at low SNR for the primary tracks of Subject 1 (Vastus Lateralis).

2.5 Conclusions

A robust SNR calculation algorithm was established to determine the effect of noise on deterministic tractography. The results showed that a minimum SNR is required for reliable quantitative analysis using tractography results and it is different for the primary and secondary eigenvectors and different algorithms. If the minimum SNR requirement is not met, variations between subjects could simply be due to variation in SNR. The minimum SNR required for repeatable tractography varies for different DTI acquisitions and muscles, and should be evaluated for each study.

Chapter 3

Reconstruction of 3D Fabric Structure and Fiber Nets in Skeletal Muscle via *in vivo* DTI

3.1   Introduction

Barriers in biological tissue, including cell membranes and connective tissue, restrict the diffusion of water making the measured diffusion tensor anisotropic. The anisotropy in the presence of barriers allows for the microstructure of tissue to be probed, making DTI a useful tool in studying organized biological tissue. Within the muscle fiber, the diffusion of water is more restricted in its cross-sectional directions than in the longitudinal direction, and thus diffuses preferentially in the direction of the fiber. The presence of a preferential direction of diffusion along the fibers manifests as the primary eigenvector, which can be used in tractography to investigate the tissue microstructure. Although the imaging voxels are much larger than individual muscle fibers, the muscle fibers are generally oriented in the same direction within the voxel, resulting in a true reconstruction of the muscle [9, 10, 52]. It has been shown that skeletal muscle tractography can be used to accurately measure the pennation angle of the gastrocnemius [7].

Apart from the primary direction of diffusion, asymmetry of the diffusion tensor on the transverse plane has been reported in the brain, heart, tongue and skeletal muscle. It is well accepted that axons in the brain have a cylindrical cross-section and any transverse asymmetry is from crossing or branching fibers [53]. The angular dispersion of the myofibers have been identified as the cause of transverse asymmetry in the tongue [54]. Transverse asymmetry in the

26

heart can be linked to studies on the myocardium revealing that the myocytes are organized into branching laminar sheets that impose organization of the myofibers into layers [55].

The axial asymmetry of the diffusion tensor in skeletal muscle has been well documented [7, 56, 57], though its cause is still unclear. Galban et al. proposed that the secondary eigenvalue is from the endomysium and the muscle fibers are organized into sheets, while the tertiary eigenvalue is related to the muscle fiber diameter and physical cross-sectional area of the muscle [56]. On the other hand, Karampinos et al. hypothesized and mathematically showed that an elliptical shape of skeletal muscle fibers can explain the asymmetry of the diffusion tensors on the transverse plane [58]. Other studies have tried to assess the difference in the secondary and tertiary eigenvalues by monitoring the variation while doing extension and contraction experiments, finding that the secondary eigenvalue stays constant while the tertiary decreases during muscle extension [59, 60].

Dissections of skeletal muscle can provide a different perspective when trying to explain the transverse asymmetry of the diffusion tensor. In a comparison of various bovine muscles, it was shown that the variation in the thickness and structure of the perimysium was much more than the variation in that of the endomysium [32]. In another study it was shown that the perimysium surrounded and separated fascicles of distinctive shapes and sizes in different muscles, while the muscle fibers inside the fascicles looked fairly similar [61]. It was observed that the cross-sectional shapes of the fascicles in the soleus and rectus femoris were not circular, but rather elongated and elliptical. Differences in the two muscles included the relative thickness of the perimysium in each direction, the staggering of fascicles relative to each other, and the elongation of the fascicles.

This work was a continuation of the findings of Karampinos et el. showing the

organization of the secondary eigenvector on a single transverse slice of the human calf [58]. It is hypothesized that the spatial organization of the secondary eigenvector can provide information regarding muscle quality. Using tractography, the 3D fabric structure of the diffusion in skeletal muscle was reconstructed and topological metrics were developed to quantify its degree of organization.

3.2   Methods

3.2.1   DTI and Tractography

The calf and thigh of various volunteers were scanned using the same DTI sequence described in chapter two with ten averages. Tractography of the primary and secondary eigenvectors were performed with Diffusion Toolkit and TrackVis software [45] using the interpolated streamline algorithm with 0.5 mm step size [4]. The angle termination criterion used for primary and secondary tracks were 25 and 30 degrees, respectively. Also, the minimum track length used for primary and secondary tracks were 20 and 15 mm, respectively. Both primary and secondary tracks had one random seed point per voxel and a B-spline filter was applied to smooth the tracts.

A high-resolution T1-weighted anatomical image was also acquired using the same slice positioning as the DTI scan. If there was subject movement between the DTI and anatomical scans, the FSL FLIRT software package [62] was used to register and align the scans. The high-resolution images were used for more accuracy while drawing the ROI, because often times the aponeurosis separating the muscles was faded and unclear on the low-resolution b_0 image from the DTI scan. All data outside the muscle was removed prior to tractography.

3.2.2 Quantitative Analysis of Fabric Structure

An algorithm was written in MATLAB (The Mathworks, Inc., Natick, MA) to sort the primary and secondary tracks into composite nets to quantify the fabric structure's organization. First a connectivity matrix was calculated by identifying all the crossing primary and secondary tracks. Tracks were considered crossing when the closest distance between the two was less than 0.3 mm. The computation time for this step was the longest, as the distance between every primary and secondary track segment was checked. After all the crossing nodes were identified, the largest defect-free rectangular net was determined and the corresponding nodes were removed from further consideration for inclusion in other nets. The algorithm was complete when all nets with a minimum of six nodes were counted. Figure 3.1 is a simplified example showing how the nets of various sizes are determined.
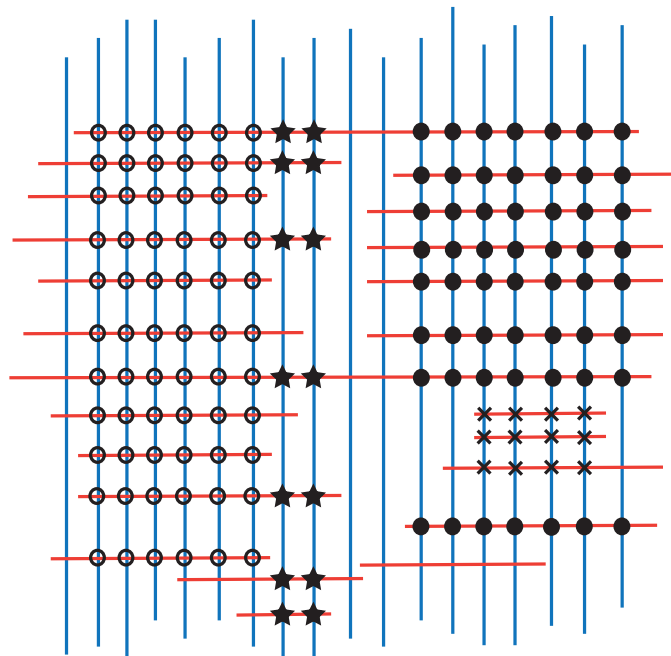

Figure 3.1: Schematic showing crossing primary (blue) and secondary (red) tracks and the identification of 66-node (open circles), 56-node (closed circles), 14-node (stars) and 12-node (Xs) rectangular nets.

By seeding the primary and secondary tracks at the center of each voxel, nodes were artificially induced. Using one random seed per voxel resolved this issue, but caused variability

in the calculation of the nets. The algorithm was executed 50 times with random seed points to determine how many averages were necessary for convergence.

The metric for quantifying the degree of organization of the fabric structure takes into account the number of nets, mean size of the nets, and volume of the muscle, and is described with the following formula (Eq. 3.1):

$$\text{Metric} = \frac{\text{Number of Nets} \ \times \ \text{Mean Net Size}}{\text{Muscle Volume}}. \tag{3.1}$$

To further establish the existence of the fabric structure and determine the repeatability of the metric, two consecutive DTI scans were performed on four subjects. The subjects did not move between the scans to completely remove the variability from slice positioning, magnetic field shimming and drawing of the ROI.

3.3   Results and Discussion

Figures 3.2 through 3.5 present the fabric structure observed in the gastrocnemius and vastus medialis, lateralis and intermedius muscles. Each track segment is colored according to anatomical orientation, where blue is superior/inferior, red is left/right, and green is anterior/posterior.

Although the secondary eigenvector has a constraint of being perpendicular to the muscle fiber, there was still organization in the transverse plane. The general orientation of the secondary tracks in these muscles was consistent across subjects, although some appeared more fragmented than others. The muscles shown in Figures 3.2 through 3.5 had some of the more organized fabric structures observed.

It is important to note that the secondary tracks do not have the same physical significance as the primary tracks. While the primary tracks reveal muscle fiber structure, the

secondary tracks simply show diffusion analogous to how streamlines are used to represent fluid flow. The secondary tracks do not represent actual fibers perpendicular to the muscle fibers, but rather the direction of less restricted diffusion.

When relating these tractography results to other studies, it seems as though the perimysium and arrangement of fascicles are responsible for the large variations in the secondary organization between muscles and subjects. We present the hypothesis that the organization of the secondary eigenvector in certain muscles is because the fascicles are organized into sheets that contract uniformly and slide past each other during contraction and extension. It is possible that the connective tissue adapts to strains in the axial direction, which gives rise to structures that restrict diffusion preferentially.
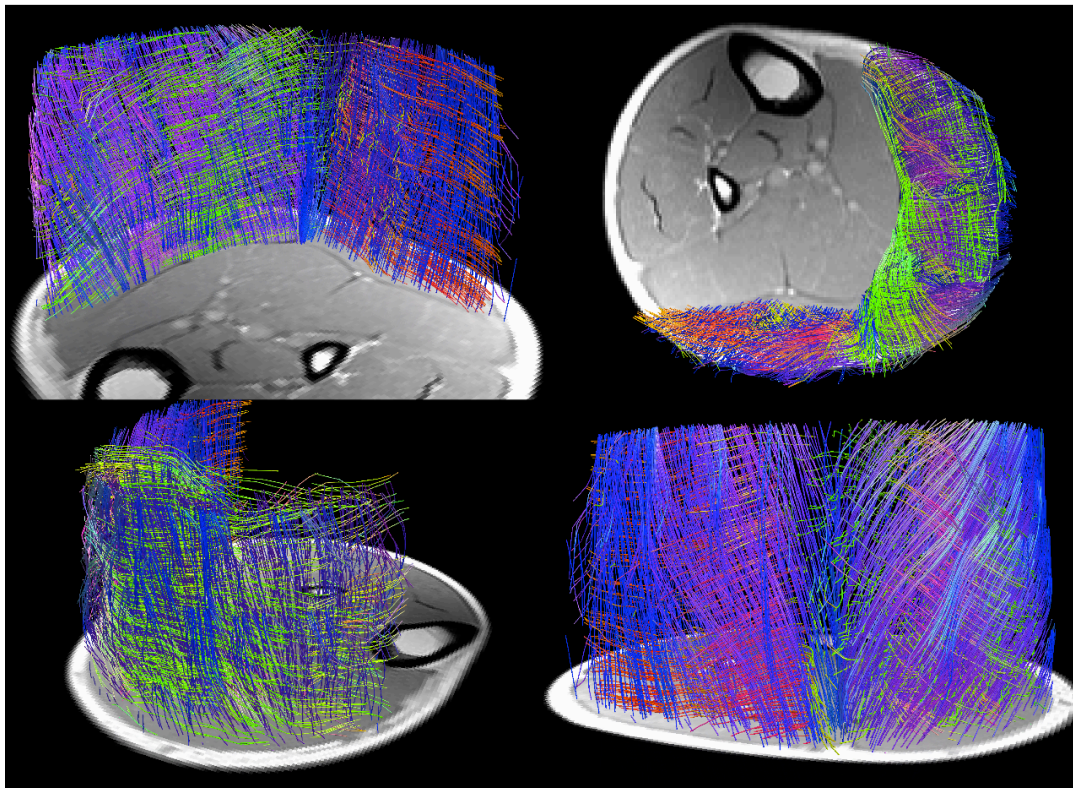

Figure 3.2: Tracking of the primary and secondary eigenvectors in the gastrocnemius medialis and lateralis.
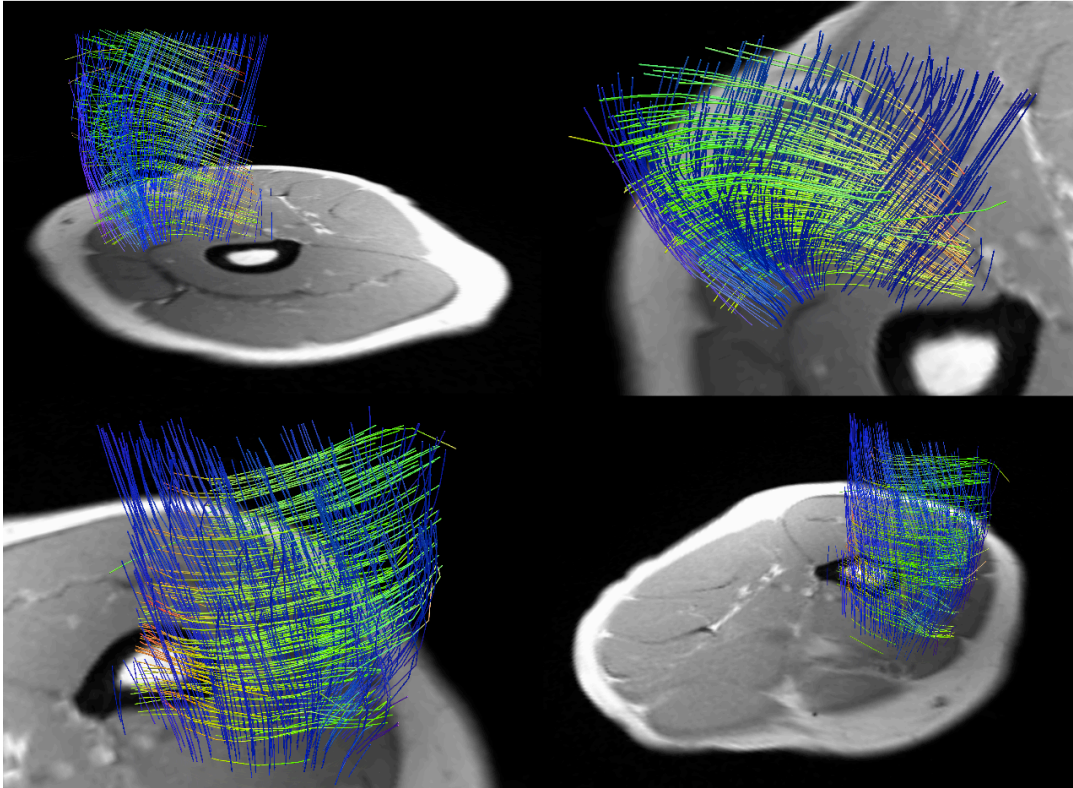
Figure 3.3: Tracking of the primary and secondary eigenvectors in the vastus medialis.
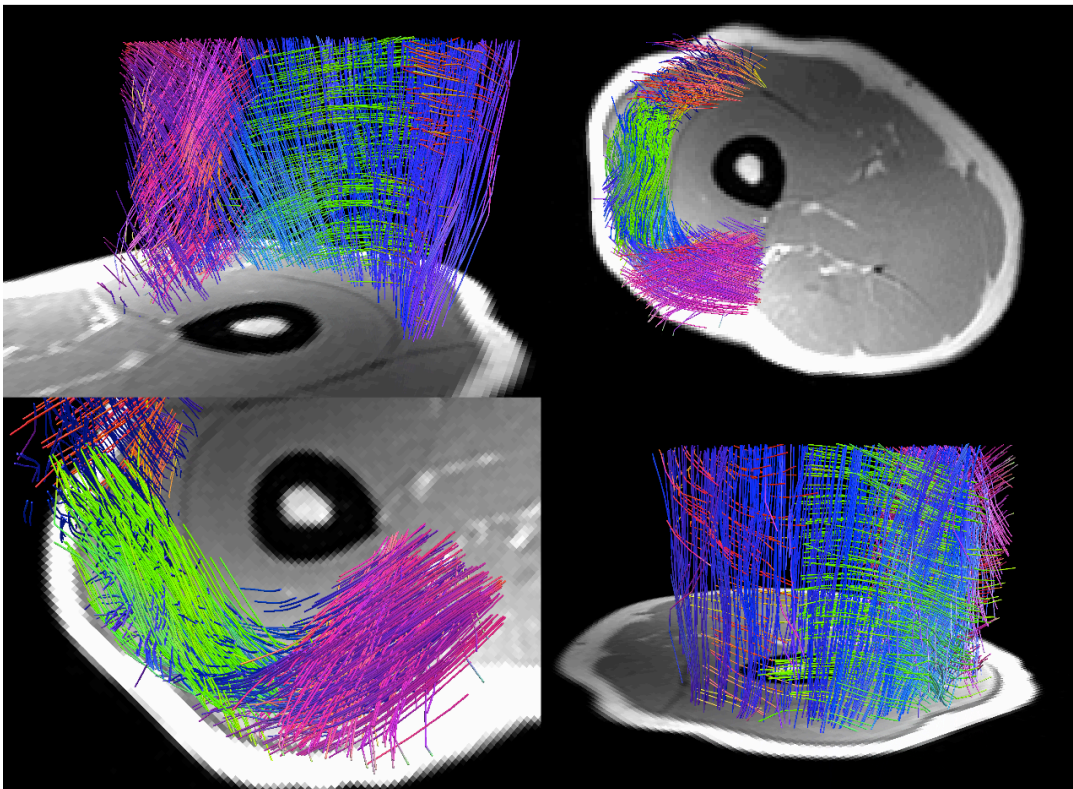
Figure 3.4: Tracking of the primary and secondary eigenvectors in the vastus lateralis.
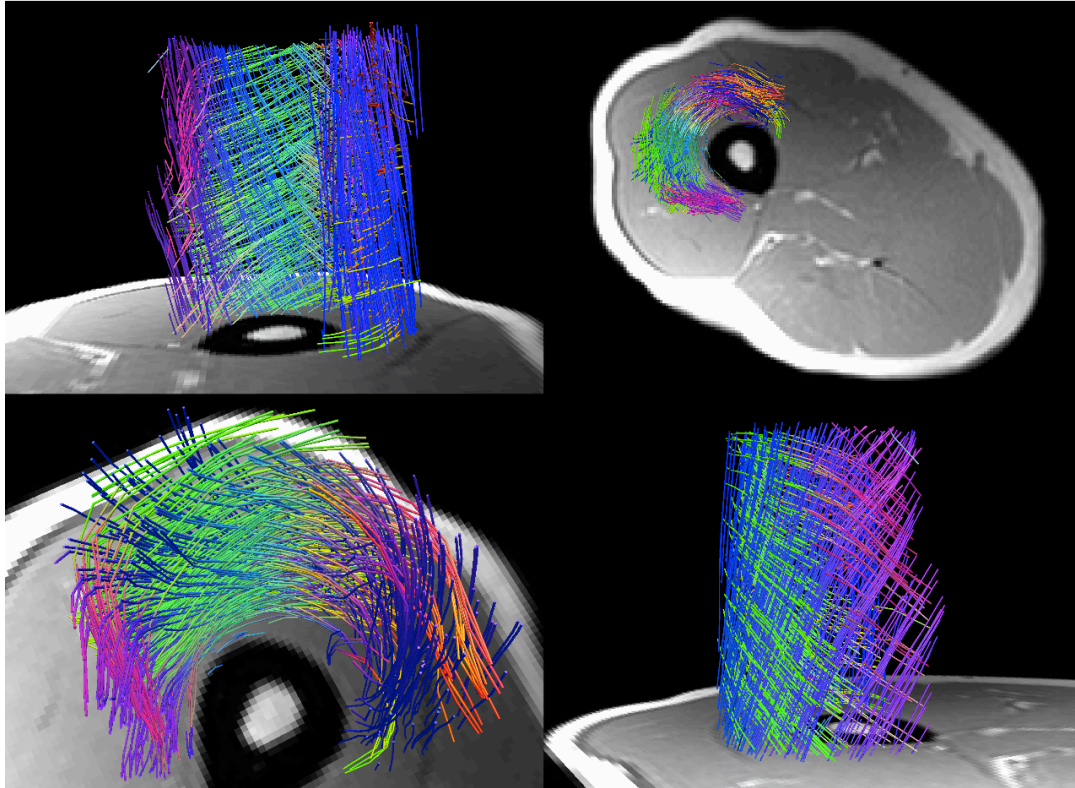
Figure 3.5: Tracking of the primary and secondary eigenvectors in the vastus intermedius.

In tractography, the tracks are started at seed points and propagate in both directions until the stop criterion is reached. Figure 3.6 was obtained by randomly seeding the primary and secondary tracks and running the tractography and net algorithms 50 times. After about 20 repetitions, the average and standard deviation converge for the number of nets and mean net size. Therefore, 20 averages were also used in the quantitative results presented in the following discussion.

To establish the fabric structure observed from the DTI measurements in muscle, two consecutive DTI scans were used, and tractography was performed on each. The results from four subjects are shown in Table 3.1, which is ordered with increasing SNR. The major contribution to the difference between consecutive scans was the number of nets. As expected, the mean net size was similar for the consecutive scans because it is an average quantity. The reproducibility of the metric was very closely related to the SNR for the scan. In chapter two, it

was shown that the primary and secondary tracks require a minimum of 16 and 35 SNR for convergence, respectively, using these same tractography and scan parameters. The results here further verify the findings of chapter two.
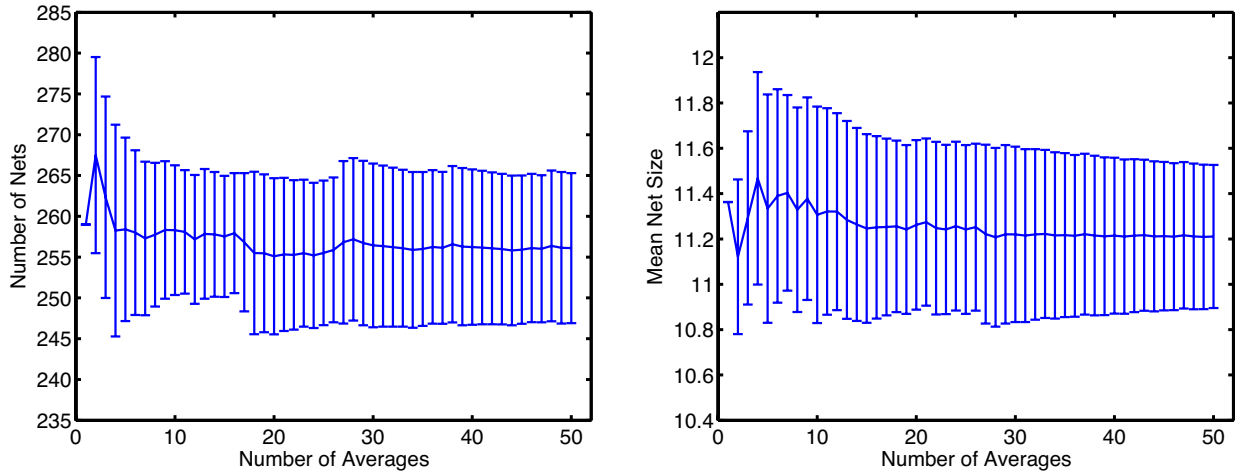
Figure 3.6: Plots showing the effect of random seeding on the number of nets and mean net size.

Table 3.1: Characterizing the repeatability of the fabric metric using consecutive DTI scans.

Subject	SNR	ROI Volume	# Nodes	# Nets	Mean Net Size	Metric	Percent Difference
1	25.44	86.6 cm^3	1200 ± 100	53 ± 7	9.0 ± 0.5	5.46	27.6 %
	24.11		1480 ± 70	72 ± 5	8.7 ± 0.3	7.20	
2	29.32	91.9 cm^3	2390 ± 120	120 ± 9	9.0 ± 0.3	11.79	10.7 %
	29.89		2560 ± 90	130 ± 7	9.2 ± 0.3	13.12	
3	28.33	180.0 cm^3	6560 ± 200	350 ± 15	9.8 ± 0.2	18.99	8.7 %
	31.95		7030 ± 160	371 ± 15	10.0 ± 0.2	20.71	
4	35.37	86.2 cm^3	2400 ± 70	124 ± 5	9.4 ± 0.3	13.52	0.2 %
	33.58		2480 ± 110	125 ± 7	9.3 ± 9.3	13.55	

3.4   Conclusions

This chapter established the existence of an organized 3D fabric structure reconstructed from DTI of human skeletal muscle. Building on previous studies, the fabric structure hints at the organization of fascicles into sheets in the gastrocnemius and vastus lateralis, medialis, and intermedius muscles. It was further hypothesized that the organization of the fabric can be related to muscle quality, and a method to quantify this was developed. A limitation of the proposed method is the high SNR required for reproducibility. Due to the nature of deterministic tractography, errors due to noise can accumulate along the track and introduce variability when trying to quantify results. The net calculation algorithm can also build on these errors, making it difficult to get repeatable results. By showing that the nets did not change for consecutive scans at high SNR indicated that the secondary structure was not an imaging artifact, but rather due to physical diffusion barriers in the muscle.

Chapter 4

Summary and Conclusions

The scope of this thesis was the investigation of utilizing diffusion tensor imaging for studying the structure of skeletal muscle *in vivo*. It is well accepted that DTI coupled with tractography can provide information about the macroscopic architecture of the muscle. Tracking of the secondary eigenvector revealed an ordered secondary structure that can be linked to the microstructural organization of connective tissue resulting in fascicles being arranged in sheets. It was hypothesized that the organization of the 3D fabric structure derived from the crossing primary and secondary tracks can correlate to muscle quality, making DTI a unique and valuable tool in non-invasively studying skeletal muscle.

While analyzing the reliability of the tractography results in relation to the signal-to-noise ratio of the diffusion images, it was observed that the anisotropy of the imaging voxels favor the primary but not the secondary tracks. The voxel dimensions used in this thesis were based on literature values and likely not ideal for tracking the secondary eigenvector. Future work should investigate how varying the voxel dimensions would affect the SNR and tractography results, and take care in ensuring the appropriate acquisition is used for the desired tracking. Future improvements in the DTI scan include decreasing the scan time and acquiring the entire muscle instead of a small section. The attempt to quantify the fabric organization by extracting rectangular nets also led to other ideas. Since deterministic tractography is sensitive to noise, the effect of noise is multiplied at each step of the post-processing analysis leading to the requirement of high SNR. The tractography algorithm could be modified to be less sensitive to

noise by employing a hybrid of deterministic and probabilistic tractography. The algorithm used

to quantify the fabric structure could also be improved, by incorporating into a finite element

model of the muscle to determine the optimal structure for force transmission. Finally, the

analysis up to this point has been on a passive, relaxed muscle. This study applied to activated or

stretched muscles could lead to improvements in the understanding of muscle function and

quality.

References

1. Heemskerk, A., et al., *Determination of mouse skeletal muscle architecture using three-dimensional diffusion tensor imaging.* Magn Reson Med, 2005. 53(6): p. 1333-1340.

2. Budzik, J.F., et al., *In vivo MR tractography of thigh muscles using diffusion imaging: initial results.* Eur Radiol, 2007. 17(12): p. 3079-3085.

3. Mori, S., et al., *Three-dimensional tracking of axonal projections in the brain by magnetic resonance imaging.* Ann Neurol, 1999. 45(2): p. 265-269.

4. Conturo, T., et al., *Tracking neuronal fiber pathways in the living human brain.* P Natl Acad Sci Usa, 1999. 96(18): p. 10422-10427.

5. Basser, P., et al., *In vivo fiber tractography using DT-MRI data.* Magn Reson Med, 2000. 44(4): p. 625-632.

6. Lazar, M., et al., *White matter tractography using diffusion tensor deflection.* Hum Brain Mapp, 2003. 18(4): p. 306-321.

7. Damon, B.M., et al., *Validation of diffusion tensor MRI-based muscle fiber tracking.* Magn Reson Med, 2002. 48(1): p. 97-104.

8. Damon, B.M., *Effects of image noise in muscle diffusion tensor (DT)-MRI assessed using numerical simulations.* Magn Reson Med, 2008. 60(4): p. 934-944.

9. Froeling, M., J. Oudeman, and S. van den Berg, *Reproducibility of diffusion tensor imaging in human forearm muscles at 3.0 T in a clinical setting.* Magn Reson Med, 2010.

10. Heemskerk, A.M., et al., *Repeatability of DTI-based skeletal muscle fiber tracking.* Nmr Biomed, 2010. 23(3): p. 294-303.

11. Kallman, D.A., C.C. Plato, and J.D. Tobin, *The role of muscle loss in the age-related decline of grip strength: cross-sectional and longitudinal perspectives.* Journal of Gerontology, 1990. 45(3): p. M82.

12. Larsson, L., G. Grimby, and J. Karlsson, *Muscle strength and speed of movement in relation to age and muscle morphology.* J Appl Physiol, 1979. 46(3): p. 451-6.

13. Aniansson, A., et al., *Impaired muscle function with aging. A background factor in the incidence of fractures of the proximal end of the femur.* Clin Orthop Relat Res, 1984(191): p. 193-201.

14. Hyatt, R.H., et al., *Association of muscle strength with functional status of elderly people.* Age Ageing, 1990. 19(5): p. 330-6.

15. Woittiez, R.D., et al., *A three-dimensional muscle model: a quantified relation between form and function of skeletal muscles.* J Morphol, 1984. 182(1): p. 95-113.

16. Blemker, S.S. and S.L. Delp, *Three-dimensional representation of complex muscle architectures and geometries.* Ann Biomed Eng, 2005. 33(5): p. 661-673.

17. Blemker, S.S., et al., *Image-based musculoskeletal modeling: Applications, advances, and future opportunities.* J Magn Reson, 2007. 25(2): p. 441-451.

18. Chi, S.-W., et al., *Finite element modeling reveals complex strain mechanics in the aponeuroses of contracting skeletal muscle.* J Biomech, 2010. 43(7): p. 1243-50.

19. Blemker, S.S., P. Pinsky, and S.L. Delp, *A 3D model of muscle reveals the causes of nonuniform strains in the biceps brachii.* J Biomech, 2005. 38(4): p. 657-665.

20. Pappas, G.P., et al., *Nonuniform shortening in the biceps brachii during elbow flexion.* J Appl Physiol, 2002. 92(6): p. 2381-9.

21. Lichtwark, G.A., K. Bougoulias, and A.M. Wilson, *Muscle fascicle and series elastic element length changes along the length of the human gastrocnemius during walking and running.* J Biomech, 2007. 40(1): p. 157-64.

22. Rowe, R.W., *Morphology of perimysial and endomysial connective tissue in skeletal muscle.* Tissue Cell, 1981. 13(4): p. 681-90.

23. Purslow, P.P. and J.A. Trotter, *The morphology and mechanical properties of endomysium in series-fibred muscles: variations with muscle length.* J Muscle Res Cell M, 1994. 15(3): p. 299-308.

24. Huijing, P., *Muscle as a collagen fiber reinforced composite: a review of force transmission in muscle and whole limb.* J Biomech, 1999. 32(4): p. 329-345.

25. Jaspers, R.T., et al., *Acute effects of intramuscular aponeurotomy on rat gastrocnemius medialis: force transmission, muscle force and sarcomere length.* J Biomech, 1999. 32(1): p. 71-9.

26. Monti, R.J., et al., *Transmission of forces within mammalian skeletal muscles.* J Biomech, 1999. 32(4): p. 371-80.

27. Purslow, P., *Intramuscular connective tissue and its role in meat quality.* Meat Sci, 2005. 70(3): p. 435-447.

28. Magid, A. and D. Law, *Myofibrils Bear Most of the Resting Tension in Frog Skeletal Muscle.* Science, 1985. 230(4731): p. 1280-1282.

29. Trotter, J.A. and P.P. Purslow, *Functional morphology of the endomysium in series fibered muscles.* J Morphol, 1992. 212(2): p. 109-22.

30. Purslow, P., *The structure and functional significance of variations in the connective tissue within muscle.* Comp Biochem Phys A, 2002. 133(4): p. 947-966.

31. Borg, T.K. and J.B. Caulfield, *Morphology of connective tissue in skeletal muscle.* Tissue Cell, 1980. 12(1): p. 197-207.

32. Light, N., et al., *The role of epimysial, perimysial and endomysial collagen in determining texture in six bovine muscles.* Meat Sci, 1985. 13(3): p. 137-149.

33. Passerieux, E., et al., *Structural organization of the perimysium in bovine skeletal muscle: Junctional plates and associated intracellular subdomains.* J Struct Biol, 2006. 154(2): p. 206-216.

34. Purslow, P.P., *Muscle fascia and force transmission.* J Bodyw Mov Ther, 2010. 14(4): p. 411-7.

35. Purslow, P.P., *Strain-induced reorientation of an intramuscular connective tissue network: implications for passive muscle elasticity.* J Biomech, 1989. 22(1): p. 21-31.

36. Le Bihan, D., et al., *Diffusion tensor imaging: Concepts and applications.* J Magn Reson, 2001. 13(4): p. 534-546.

37. Basser, P. and D. Jones, *Diffusion-tensor MRI: theory, experimental design and data analysis - a technical review.* Nmr Biomed, 2002. 15(7-8): p. 456-467.

38. Stejskal, E., *Use of Spin Echoes in a Pulsed Magnetic‐Field Gradient to Study Anisotropic, Restricted Diffusion and Flow.* The Journal of Chemical Physics, 1965. 43: p. 3597.

39. Tanner, J., *Self diffusion of water in frog muscle.* Biophys J, 1979.

40. Mori, S. and P. van Zijl, *Fiber tracking: principles and strategies - a technical review.* Nmr Biomed, 2002. 15(7-8): p. 468-480.

41. Parker, G., H. Haroon, and C. Wheeler-Kingshott, *A framework for a streamline-based probabilistic index of connectivity (PICo) using a structural interpretation of MRI diffusion measurements.* J Magn Reson, 2003. 18(2): p. 242-254.

42. Behrens, T.E.J., et al., *Probabilistic diffusion tractography with multiple fibre orientations: What can we gain?* Neuroimage, 2007. 34(1): p. 144-155.

43. Dyrby, T.B., et al., *Validation of in vitro probabilistic tractography.* Neuroimage, 2007. 37(4): p. 1267-1277.

44. Jones, D.K., *Tractography gone wild: Probabilistic fibre tracking using the wild bootstrap with diffusion tensor MRI.* Ieee T Med Imaging, 2008. 27(9): p. 1268-1274.

45. Wang, R., et al., *Diffusion toolkit: A software package for diffusion imaging data processing and tractography.* Intl Soc Mag Reson Med 15, 2007.

46. Chen, B. and E. Hsu, *Noise removal in magnetic resonance diffusion tensor imaging.* Magn Reson Med, 2005. 54(2): p. 393-401.

47. Aja-Fernandez, S., et al., *Restoration of DWI data using a Rician LMMSE estimator.* Ieee T Med Imaging, 2008. 27(10): p. 1389-1403.

48. Aja-Fernandez, S., C. Alberola-Lopez, and C.-F. Westin, *Noise and signal estimation in magnitude MRI and Rician distributed images: A LMMSE approach.* Ieee T Image Process, 2008. 17(8): p. 1383-1398.

49. Coulon, O., D. Alexander, and S. Arridge, *Diffusion tensor magnetic resonance image regularization.* Med Image Anal, 2004. 8(1): p. 47-67.

50. Kwon, K., et al., *Regularization of DT-MR images using a successive Fermat median filtering method.* Phys Med Biol, 2008. 53(10): p. 2523-2536.

51. Dietrich, O., et al., *Measurement of signal-to-noise ratios in MR images: Influence of multichannel coils, parallel imaging, and reconstruction filters.* J Magn Reson, 2007. 26(2): p. 375-385.

52. Kermarrec, E., et al., *In Vivo Diffusion Tensor Imaging and Tractography of Human Thigh Muscles in Healthy Subjects.* Am J Roentgenol, 2010. 195(5): p. W352-W356.

53. Lazar, M., J. Lee, and A. Alexander, *Axial asymmetry of water diffusion in brain white matter.* Magnet Reson Med, 2005. 54(4): p. 860-867.

54. Wedeen, V., et al., *Demonstration of primary and secondary muscle fiber architecture of the bovine tongue by diffusion tensor magnetic resonance imaging.* Biophys J, 2001. 80(2): p. 1024-1028.

55. Dou, J., et al., *Combined diffusion and strain MRI reveals structure and function of human myocardial laminar sheets in vivo.* Magnet Reson Med, 2003. 50(1): p. 107-113.

56. Galban, C., et al., *Diffusive sensitivity to muscle architecture: a magnetic resonance diffusion tensor imaging study of the human calf.* Eur J Appl Physiol, 2004. 93(3): p. 253-262.

57. Sinha, S., U. Sinha, and V.R. Edgerton, *In vivo diffusion tensor imaging of the human calf muscle.* J Magn Reson, 2006. 24(1): p. 182-190.

58. Karampinos, D.C., et al., *Myofiber Ellipticity as an Explanation for Transverse Asymmetry of Skeletal Muscle Diffusion MRI In Vivo Signal.* Ann Biomed Eng, 2009. 37(12): p. 2532-2546.

59. Deux, J.F., et al., *Assessment of calf muscle contraction by diffusion tensor imaging.* Eur Radiol, 2008. 18(10): p. 2303-2310.

60. Hatakenaka, M., et al., *Alteration of proton diffusivity associated with passive muscle extension and contraction.* J Magn Reson, 2008. 27(4): p. 932-937.

61. Sharafi, B. and S.S. Blemker, *A micromechanical model of skeletal muscle to explore the effects of fiber and fascicle geometry.* J Biomech, 2010. 43(16): p. 3207-3213.

62. Jenkinson, M. and S. Smith, *A global optimisation method for robust affine registration of brain images.* Med Image Anal, 2001. 5(2): p. 143-156.